Optical nonreciprocity and hyperbolicity in altermagnetic MnF_2

Tian-Hui Li(李田慧), Yang He(何洋), Zi-Jiang Zhang(张子健), Yu Zhou(周昱), Meng-Nan Chen(陈梦南), Huai-Qiang Wang(王怀强), Meng-Dan Zhao(赵梦丹)

Citation: Chin. Phys. B. 35, 107803 (2026). DOI: 10.1088/1674-1056/ae2c68 | CSTR: 32038.14.CPB.ae2c68
http://cpb.iphy.ac.cn; http://iopscience.iop.org/cpb

What follows is a list of articles you may be interested in

Electrodynamics of a prototypical altermagnetic compound MnTe

Bixia Gao(高碧霞), Yixuan Luo(罗伊轩), Liye Cao(曹立叶), Tao Sun(孙涛), Zehao Yu(于泽浩), Lei Wang(王蕾), Xinyu Zhang(张新雨), Hongbo Hu(胡宏波), Yanfeng Guo(郭艳峰), Rongyan Chen(陈荣艳)
Chin. Phys. B. 35, 037801 (2026). DOI: 10.1088/1674-1056/ae2abc | CSTR: 32038.14.CPB.ae2abc

Josephson diode effect in altermagnet-based s-wave superconductor junction

Yi Jiang(蒋易), Han-Lin Liu(刘翰林), Jun Wang(汪军)
Chin. Phys. B. 34, 107803 (2025). DOI: 10.1088/1674-1056/add7aa | CSTR: 32038.14.CPB.add7aa

Plasmonic properties of graphene on uniaxially anisotropic substrates

Shengchuan Wang(汪圣川), Bin You(游斌), Rui Zhang(张锐), Kui Han(韩奎), Xiaopeng Shen(沈晓鹏), Weihua Wang(王伟华)
Chin. Phys. B. 30, 037801 (2021). DOI: 10.1088/1674-1056/abd168

Extinction mechanisms of hyperbolic h-BN nanodisk

Runkun Chen(陈闰堃), Jianing Chen(陈佳宁)
Chin. Phys. B. 29, 057802 (2020). DOI: 10.1088/1674-1056/ab8898

Engineering optical gradient force from coupled surface plasmon polariton modes in nanoscale plasmonic waveguides

Jiahui Lu(卢佳慧), Guanghui Wang(王光辉)
Chin. Phys. B. 25, 117804 (2016). DOI: 10.1088/1674-1056/25/11/117804

Optical nonreciprocity and hyperbolicity in altermagnetic MnF_2

Tian-Hui Li(李田慧)[1,†], Yang He(何洋)[1,†], Zi-Jiang Zhang(张子健)[1], Yu Zhou(周昱)[1,‡], Meng-Nan Chen(陈梦南)[1], Huai-Qiang Wang(王怀强)[2], and Meng-Dan Zhao(赵梦丹)[1,§]

[1] *School of Science, Hangzhou Dianzi University, Hangzhou* 310018, *China*
[2] *School of Physical Science and Technology, Nanjing Normal University, Nanjing* 210023, *China*

(Received 15 August 2025; revised manuscript received 23 November 2025; accepted manuscript online 15 December 2025)

Altermagnets have zero net magnetization but possess time-reversal symmetry breaking and non-relativistic spin-split band structures. Such materials may exhibit anomalous Hall conductivities without applying static magnetic fields. In this paper, we investigate the optical properties of the altermagnet MnF_2. The full conductivity tensor has been calculated using density functional theory and then converted into permittivities. The off-diagonal terms may slightly affect the optical responses, but the main optical properties are determined by the diagonal ones. Due to intrinsic time-reversal symmetry breaking, optical nonreciprocity has been found by polarization conversion during reflection. After hole doping, altermagnetic MnF_2 exhibits hyperbolic responses. Numerical simulations based on the finite element method have been used to confirm such hyperbolicity. Our investigations have revealed that some altermagnets may be more easily verified through optical detection and have fascinating applications in optics, which might lead to nonmagnetic material-based magneto-optical devices without external magnetic fields.

Keywords: altermagnetism, hyperbolicity, nonreciprocity

PACS: 78.20.Ls, 75.70.–I, 78.20.–e

DOI: 10.1088/1674-1056/ae2c68 **CSTR:** 32038.14.CPB.ae2c68

Recently, a new class of magnetic order called altermagnetism has been discovered, where the materials have vanishing magnetization like antiferromagnets but spin-split band structures similar to ferromagnets.[1–3] The material lacks inversion symmetry and two magnetic sublattices are related by crystal symmetry other than inversion.[4] The arrangement of other nonmagnetic atoms is crucial to such symmetry breaking. Many expected properties such as spin currents,[5] spin-splitting torque phenomena,[6,7] extraordinary magnetoelectric couplings,[8–11] and broken Kramer's degeneracy have been discovered in altermagnets.[12,13] Despite their potential applications in spintronics, altermagnets also show rich optical responses in the infrared as well as visible range. Due to time-reversal symmetry breaking, they exhibit anomalous Hall conductivities (AHCs).[14,15] Such AHC is promised by symmetry breaking, and it should be robust and can be observed even after significant charge doping. AHC is anti-symmetric and can lead to magneto-optical responses such as polarization rotation of the incident light. Thus, altermagnets which have AHC and zero magnetization may lead to magneto-optical applications without applying external magnetic fields.

Although the off-diagonal terms in the conductivity tensor such as AHC may affect the optical responses of materials, the main optical responses are determined by the diagonal ones (in the principal axes). Optical responses in materials are better understood from their permittivity tensors. The optical conductivities should be converted into permittivities based on which one can easily divide the materials into three classes: dielectric if all three-diagonal terms are positive, metallic if all three-diagonal terms are negative, and hyperbolic.[16] Hyperbolic materials have wide applications in nanophotonics such as spontaneous emission enhancement,[17,18] subwavelength imaging,[19–21] and negative refraction.[22] In the last decades, tremendous efforts have been put into designing and fabricating artificial hyperbolic materials, and delicate structures made by metals and dielectrics have been proposed which can effectively have optical hyperbolicity.[16] In recent years, researchers have started to look for hyperbolic responses in natural materials. Many kinds of materials, ranging from dielectric to metallic, have been found to possess such extreme anisotropic responses, such as hBN, BP, bAsP, MgB_2, Bismuth, and so on.[23]

MnF_2 is a dielectric which has recently been proposed as an altermagnet.[24] Calculations based on density functional theory indeed show spin-split band structures without including spin–orbit coupling (SOC). Two Mn atoms have antiparallel magnetic moments which are connected by crystal-rotation plus translation symmetry. Based on the magnetic force theorem, Chen *et al.* have calculated the dispersion relations of the magnons and indeed found in theory the split dispersions

[†]These authors contributed equally to this work.
[‡]Corresponding author. E-mail: yzhou@hdu.edu.cn
[§]Corresponding author. E-mail: Zmengdan_2017@163.com

© 2026 Chinese Physical Society and IOP Publishing Ltd. All rights, including for text and data mining, AI training, and similar technologies, are reserved.

of chiral magnons.[24] However, recent inelastic neutron scattering results on MnF_2 indicate that such splitting is negligibly small.[25] Such an experiment has not completely ruled out the possibility, as magnon dispersion splitting is only one aspect of PT symmetry breaking. In theory, MnF_2 is an altermagnet; other ways of detection might be needed to further verify such a conclusion. Apart from the split dispersions of chiral magnons, the existence of Hall conductivity which is antisymmetric provides another solid evidence for altermagnetism. Hall conductivity can lead to nonreciprocal transmission as well as reflection of electromagnetic waves which cannot happen in Néel antiferromagnets. We believe that optical detection of the PT symmetry breaking in MnF_2 is more sensitive and might tell us whether it is an altermagnet or not.[26,27]

In this paper, we investigate the optical properties of the altermagnet MnF_2 using density functional theory (DFT). The band structures have been calculated and then used to obtain the maximally localized Wannier functions from which the tight-binding Hamiltonian and physical properties can be derived. The frequency-dependent full conductivity tensor has been calculated based on velocity operators which also include transverse responses and can take into account the anomalous Hall effect. We have then converted the conductivities into permittivities using the well-known formula. Although the off-diagonal terms in the permittivity tensor are small, they are all kept in this paper. To explore optical applications, the guided modes in square cross-sectional MnF_2 strips have been calculated using numerical approaches. The electric fields are found to be slightly twisted due to the existence of off-diagonal terms in the permittivity tensor. Due to the intrinsic time-reversal symmetry breaking, optical nonreciprocity has been demonstrated based on the calculation of the polarization conversion during reflection. After hole doping, the permittivity along the *c*-axis becomes negative while the permittivities along the *a*-axis and *b*-axis are positive, corresponding to the case of hyperbolicity in a particular frequency range. The off-diagonal terms can only slightly affect the optical responses and are not deterministic. Numerical simulations based on the finite element method have been used to confirm the hyperbolicity, where the full permittivity tensor has been used. Our investigations indicate that altermagnets have huge potential in optical applications and may lead to nonmagnetic material-based magneto-optical devices without external magnetic fields.

The calculations of the density functional theory have been performed within quantum espresso,[28–30] using optimized norm-conserving Vanderbilt pseudopotentials.[31] The exchange–correlation functional is LDA and the Hubbard parameter in DFT+U (Dudarev's formulation) is 5 eV for 3d electrons in Mn. The cutoff energies for density and wavefunctions are 360 Ry and 90 Ry, respectively. The Monkhorst–Pack grid is $25 \times 25 \times 37$. Figure 1(a) shows the structure of MnF_2 where purple and green spheres indicate the Mn and F atoms, respectively. Two Mn atoms have anti-parallel magnetic moments denoted by the red and blue arrows, respectively. Two Mn atoms are nonequivalent due to their chemical bonds to F atoms and the magnetic moments. Figure 1(b) shows the Brillouin zone where high-symmetry points are marked. The band structures are calculated along the red lines in Fig. 1(b) and shown in Fig. 1(c) where spin–orbit coupling is not included. The spin splitting is obvious. The highest valence band is rather flat along the *GXMG* path as shown by the shaded area in Fig. 1(c), but it has a large slope along the *GZ* path, which indicates rich optical phenomena in this area. Flat band dispersion indicates a large effective mass of electron and small plasmon frequency, which can lead to positive total permittivity in a particular optical frequency range. The band structures are then projected onto orthogonal atomic s, p, and d orbitals, and the results are shown in Fig. 1(d). Obviously, p orbitals in F atoms and d orbitals in Mn atoms contribute most to the band structures. The d orbital is usually localized, which can explain the flat region in Fig. 1(c). It might be surprising that s orbitals in Mn are important here. The anomalous Hall conductivity at zero frequency can be calculated from the valence bands. However, conduction bands are required here since we are concerned about the frequency-dependent anomalous Hall conductivities; thus, s, p, and d orbitals should all be included in the calculation. The contributions of s orbitals in F atoms and p orbitals in Mn atoms are relatively small and not plotted here.

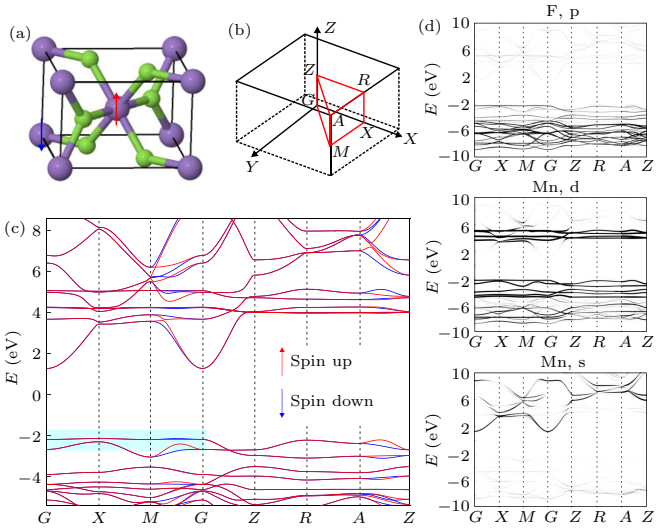

Fig. 1. (a) Crystal structure of MnF_2, where purple and green spheres indicate Mn and F atoms, respectively. Red and blue arrows indicate the magnetic moments of Mn atoms. (b) Brillouin zone where the red lines denote the *k*-path on which we plot the bands. (c) Band structure of MnF_2, where red and blue curves respectively indicate the spin-up and spin-down channels. Shaded area denotes flat band, indicating rich optical phenomena after hole doping. (d) From top to bottom, the p-orbital projection of bands for F atom, the d-orbital projection of bands for Mn atom, the s-orbital projection of bands for Mn atom.

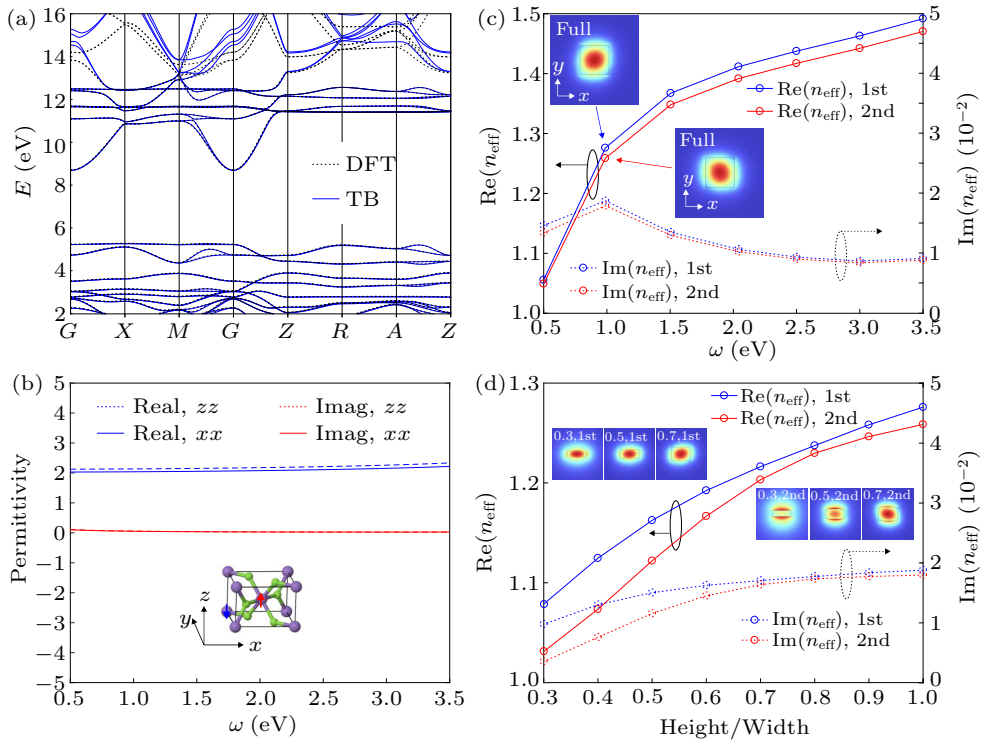

Fig. 2. (a) The band structure reconstructed from the tight-binding Hamiltonian within Wannier90 is plotted with solid blue curves, which is nearly identical to the results from DFT (plotted with black dashed curves), especially in the energy range regarding the optical transitions in this paper. (b) The diagonal components of the permittivity tensor are plotted, due to the structure, $\varepsilon_{xx} \approx \varepsilon_{yy} < \varepsilon_{zz}$. Inset shows the crystal structure in Cartesian coordinates. (c) Effective indices of the first two guided modes in MnF_2 strip with 1 μm-wide square cross section. (d) Effective indices of the first two guided modes as functions of the height/width ratio. Insets are the field profiles $|E|$.

To calculate the optical conductivities, maximally localized Wannier functions (MLWFs) have been derived using the Wannier90 package.[32] The band structures are recalculated with spin–orbit coupling and then projected onto these localized functions with spin-up and spin-down channels. For accuracy, s and p orbitals of F atoms and s, p, and d orbitals of Mn atoms are all used to construct the initial guess of the MLWFs, and the valence bands and part of the conduction bands are kept frozen. The Monkhorst–Pack grid for constructing MLWFs is $10 \times 10 \times 14$. At the end of this procedure, one gets the localized Wannier functions as well as the tight-binding Hamiltonian. The band structures can be reconstructed from these WFs, as shown in Fig. 2(a), where dashed black and blue solid curves are the results from DFT and WFs, respectively. In the energy range we are concerned with, they are almost identical. The tight-binding Hamiltonian obtained above can be used to calculate the conductivities. The optical conductivities have been evaluated using TBPLaS as[33]

$$\sigma_{ij}(\hbar\omega) = \frac{\mathrm{i}e^2\hbar}{N_k\Omega_c}\sum_{k,m,n} \times \frac{\langle\phi_{n,k}|v_i|\phi_{m,k}\rangle\langle\phi_{m,k}|v_j|\phi_{n,k}\rangle}{\epsilon_{m,k}-\epsilon_{n,k}+(\hbar\omega+\mathrm{i}\eta)}\Delta f_{mnk}, \quad (1)$$

where $\Delta f_{mnk} = (f_{m,k} - f_{n,k})/(\epsilon_{m,k} - \epsilon_{n,k})$, $ij = x, y, z$, N_k is the total k number and Ω_c is the volume of the cell. $\epsilon_{m,k}$ and $\phi_{m,k}$ are eigenvalues and eigenstates, and v_i is the velocity operator.[33] The k-mesh is $21 \times 21 \times 31$ and $\eta = 50$ meV. The conductivities are then converted into permittivities. The off-diagonal terms are rather small in the frequency range we are interested in and are not shown here. The permittivities ε_{zz} and ε_{xx} are plotted in Fig. 2(b), where the inset shows the coordinates. The permittivity ε_{zz} along the c-axis is slightly larger than those in the other two orthogonal directions and $\varepsilon_{xx} \approx \varepsilon_{yy}$. Small imaginary parts in permittivities are due to the imaginary energy (broadening) used during the calculations. Actually, conductivities can also be calculated based on the WFs and Kubo formula within the Wannier90 package, and then converted into permittivities; however, no qualitative differences have been found. To explore the optical applications, we decide to find the guided modes in an MnF_2 strip with square cross-section whose width is 1 μm. The complex effective indices have been numerically calculated using the commercial software package COMSOL[34] and only the lowest two modes are plotted in Fig. 2(c) for clarity. The optical loss comes from the broadening we used to calculate the conductivities; thus, it is phenomenological. The insets are the field profiles of the modes at $\omega = 0.9878$ eV from which one can clearly see that the fields are little twisted due to the off-diagonal components in the permittivity tensor. These off-diagonal permittivities are small but can not be omitted in the consideration of the optical properties. Since $\varepsilon_{xx} \approx \varepsilon_{yy}$ the electric fields of the modes are not confined at the cor-

ners of the square and the dispersion relations split into two branches, as shown by the red and blue curves in Fig. 2(c). If we force $\varepsilon_{xx} = \varepsilon_{yy}$, the field profiles would be totally different and the two modes are degenerate. Thus, mode splitting is caused by small differences of the permittivities along a and b axes. We have further varied the height/width ratio of the cross-section and calculated the modes at $\omega = 0.9878$ eV as shown in Fig. 2(d), where insets are the field profiles. As the ratio decreases, the splitting of the two modes becomes smaller at first and then larger, indicating the existence of the off-diagonal terms where the principal axes are not along x and y directions. These rich optical phenomena indicate that MnF_2 is an anisotropic dielectric and has potential applications in nanophotonics.

The permittivity can be calculated from conductivity as

$$\varepsilon_{ij}(\omega) = \delta_{ij} + \mathrm{i}\sigma_{ij}(\omega)/\omega\varepsilon_0, \tag{2}$$

where δ_{ij} is the Kronecker delta function, $\sigma_{ij}(\omega)$ is the three-dimensional conductivity, and ε_0 is the vacuum permittivity. Below, the conductivities calculated using the adaptive smearing technique within the Wannier90 package have been used, and three off-diagonal components ε_{xy}, ε_{yz}, and ε_{zx} in pristine MnF_2 are plotted in Fig. 3(a). ε_{xy} and also ε_{yx} are the dominant off-diagonal components corresponding to the fact that the magnetic moments of Mn atoms are along the z axis. Two diagonal components ε_{xx} and ε_{zz} of the permittivity tensor are plotted in Fig. 3(b). With large photon energy, interband transition happens and the material becomes optically lossy. Since the gap is about 4 eV, this material is dielectric at low photon energies. After being doped with positive charges, the Fermi level shifts towards the valence bands, which may lead to interesting optical responses. Figure 3(c) shows the off-diagonal components ε_{xy}, ε_{yz}, and ε_{zx} for $E_F = 5.2717$ eV corresponding to roughly 0.07 extra positive charges added in the cell (about 10^{20} cm^{-3} carrier density) during DFT calculations; the diagonal components are plotted in Fig. 3(d). Please note that if one uses other kinds of pseudopotentials, the corresponding charges would drastically change; *i.e.*, it does not correspond to the value which actually should be used in experiments. Slightly doping the material with holes can lead to resonant peaks in the ultraviolet range as well as decreasing/increasing of the real/imaginary part of ε_{zz} at very low frequencies indicated by the inset in Fig. 3(d). Resonant peaks cannot change the reflection of light and polarization conversion very much as shown below. To show the magneto-optical responses, we have numerically calculated the polarization conversion of the magneto-optical Kerr effect and demonstrated optical nonreciprocity using COMSOL. The full permittivity tensor corresponding to the lightly hole-doped MnF_2 as shown in Figs. 3(c) and 3(d) has been used. We focus on the polarization conversion, *i.e.*, r_{sp} and r_{ps}, where s and p respectively denote the transverse electric and transverse magnetic polarizations.

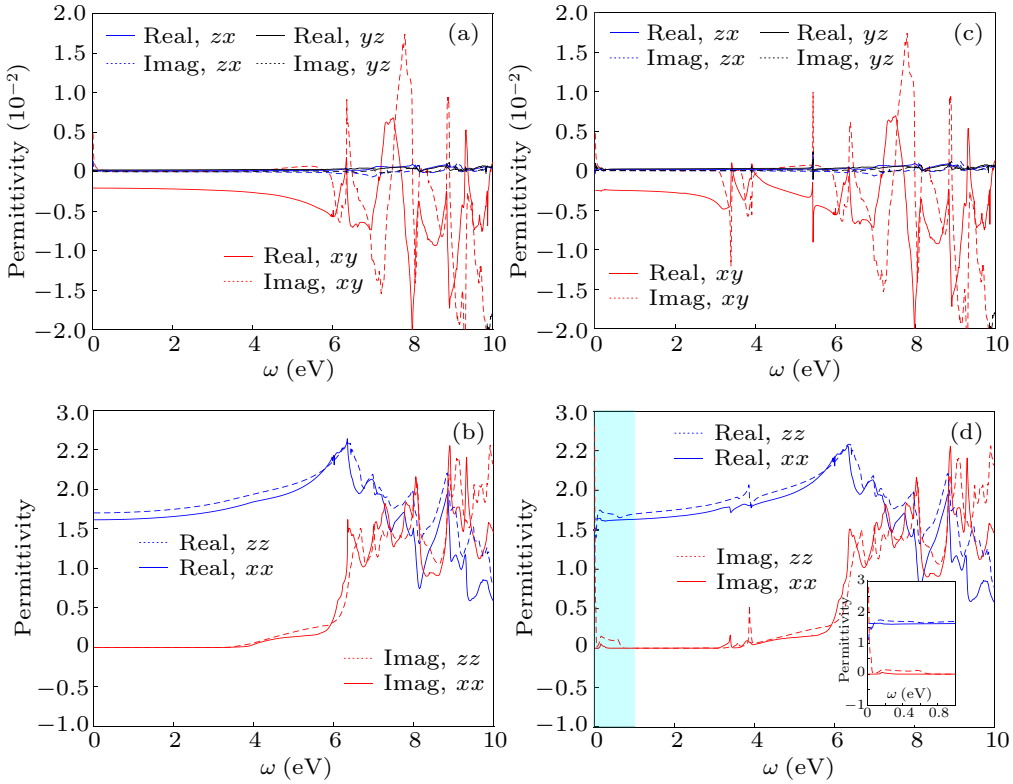

Fig. 3. (a) Three off-diagonal components ε_{xy}, ε_{yz}, and ε_{zx} and (b) two diagonal components ε_{xx} and ε_{zz} of the permittivity tensor in pristine MnF_2. (c) Three off-diagonal components ε_{xy}, ε_{yz}, and ε_{zx} and (d) two diagonal components ε_{xx} and ε_{zz} of the permittivity tensor in lightly hole-doped MnF_2, where $E_F = 5.2717$ eV corresponding to roughly 0.07 extra positive charges in the cell during DFT calculations. Inset is the zoomed-in plot of the shaded region.

Figures 4(a) and 4(b) are $|r_{sp}|$ and $|r_{ps}|$ under various incident angles $\alpha = 0°, 30°, 60°, -60°$, where the c-axis is parallel to the surface (insets show the corresponding schematics). The polarization conversion effect is obvious. When the c-axis is vertical to the surface, $|r_{sp}|$ and $|r_{ps}|$ become much larger, as shown in Figs. 4(c) and 4(d). The nonreciprocity is indicated by $r_{sp}(\alpha = 60^{\circ}) \neq r_{ps}(\alpha = -60^{\circ})$, and please note that MnF_2 now has zero net magnetization and such nonreciprocity is caused by the intrinsic PT symmetry breaking, unlike those depending on external magnetic fields.[35] Using high-accuracy optical instruments, differences in the coefficients as small as 0.04 are fully detectable. Also, as shown in Figs. 4(e) and 4(f), $|r_{sp}|$ and $|r_{ps}|$ are calculated for the case where the c-axis is parallel to the surface and a- and b-axes (respectively indicated by the red and blue arrows in the insets) are rotated by 45 degrees being symmetrical to the light incident plane. The nonreciprocity is again indicated by the differences in the coefficients. It is worth mentioning that r_{sp} and r_{ps} of KV_2Se_2O which is also an altermagnet are about 10^{-6}; MnF_2 has a much larger polarization conversion effect because it has relatively low refractive indices and is suitable for optical detection of altermagnetism.

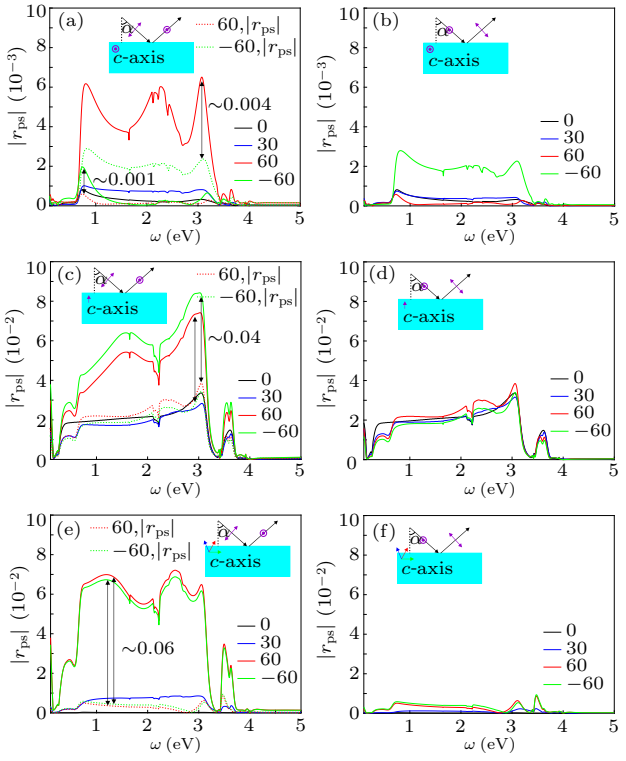

Fig. 4. Polarization conversion in reflection: (a) $|r_{sp}|$ and (b) $|r_{ps}|$; under various incident angles, where the c-axis is parallel to the surface; (c) $|r_{sp}|$ and (d) $|r_{ps}|$ under various incident angles, where the c-axis is vertical to the surface; (e) $|r_{sp}|$ and (f) $|r_{ps}|$ under various incident angles, where the c-axis is parallel to the surface and the a- and b-axes are rotated by 45 degrees, as shown by the insets. Nonreciprocity is indicated by $r_{sp}(\alpha = 60°) \neq r_{ps}(\alpha = -60°)$ indicated by the black double arrows in Figs. 4(a), 4(c), and 4(e).

Due to the anisotropy, hyperbolic optical response might be found in MnF_2 after being heavily hole-doped. Below we have assumed that the magnetic structure of MnF_2 is unchanged. The Fermi energy has been shifted to intersect with the valence bands and the corresponding optical conductivities have been calculated using a $21 \times 21 \times 31$ k-mesh with an adaptive refinement of $5 \times 5 \times 5$. These conductivities are again evaluated within the Wannier90 package using an adaptive scheme for broadening. For Fermi energy $E_F = 5$ eV, the $\sigma_{xx}(\omega)$ and $\sigma_{zz}(\omega)$ are plotted in Fig. 5(a), where peaks correspond to the interband transition of electrons. The derived permittivities are plotted in Fig. 5(b). With hole doping, the permittivities become negative at low frequencies. The optical responses are mainly determined by the diagonal terms, and one can see that at low frequencies (the frequency range denoted as A) this material is optically metallic with anisotropy. At relatively high frequencies, the permittivities are positive, indicating in this frequency range (denoted as C) the material is optically dielectric. Due to huge differences in slopes in the band structures, within some frequency range (denoted as B) the permittivity along the c-axis firstly becomes negative while the ones along other two directions remain positive, corresponding to hyperbolic responses where the isofrequency contour of electromagnetic waves is hyperboloid. Such hyperbolicity can be ascribed to the localized d orbitals in Mn atoms that contribute most to the valence bands in the shaded area in Fig. 1(c). We have further changed the Fermi energy to 4.74 eV, and the conductivities and permittivities are plotted in Figs. 5(c) and 5(d). Apart from the three regions mentioned above, another frequency range denoted as D also indicates hyperbolic optical responses. Such hyperbolicity accompanied with larger losses is caused by interband transition of electrons. The transition dipole is so strong that the effective permittivity becomes negative.

To directly confirm the hyperbolicity, numerical simulations have been performed using COMSOL. An electric dipole has been put at the surface of an MnF_2 slab with its orientation parallel to the surface, as shown by the bidirectional arrows in Figs. 5(e) and 5(f). We have simulated the radiation of the fields at four different frequencies: $\omega = 0.6$ eV, $\omega = 0.83$ eV, $\omega = 0.96$ eV, and $\omega = 1$ eV. In the case of $E_F = 5$ eV as shown in Fig. 5(e), $\omega = 0.83$ eV and $\omega = 0.96$ eV correspond to hyperbolicity and the electric field patterns can be clearly identified with hyperbolic features. In the case of $E_F = 4.74$ eV as shown in Fig. 5(f), only $\omega = 0.83$ eV corresponds to hyperbolicity. Hyperbolic responses are ascribed to the flat region of the valence bands, which indicates the robustness of such a phenomenon. Even when MnF_2 becomes ferromagnetic, hyperbolicity still exists since both spin-up and spin-down conductivities contribute to the total longitudinal conductivity and the d orbitals of Mn atoms still give flat band dispersions.

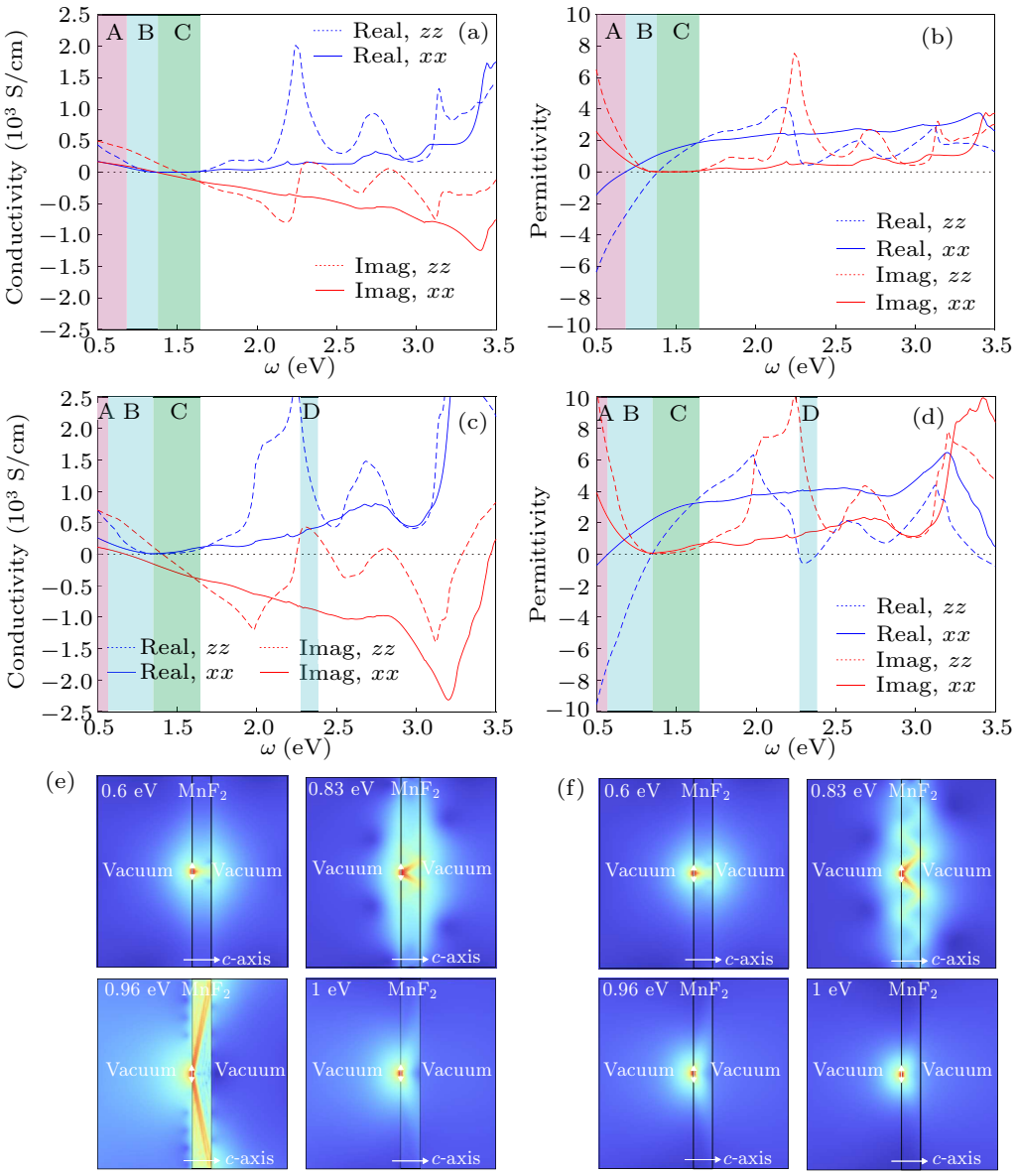

Fig. 5. (a) The conductivities σ_{xx} and σ_{zz}, and (b) the permittivities ε_{xx} and ε_{zz} when $E_F = 5$ eV. There are three frequency ranges denoted as A, B, and C, showing metallic, hyperbolic, and dielectric responses, respectively. (c) The conductivities σ_{xx} and σ_{zz}, and (d) permittivities ε_{xx} and ε_{zz}, when $E_F = 4.74$ eV. Despite the three frequency regions mentioned before, there also exists a frequency range with hyperbolic responses marked as D. Electromagnetic waves excited by an electric dipole near MnF_2 slab surface, plotted as $\log_{10}(|E|)$, when (c) $E_F = 5$ eV and (d) $E_F = 4.74$ eV. The photon energy is denoted in the figures.

In conclusion, we have theoretically investigated the optical properties of MnF_2, which has been claimed to have altermagnetism. The band structures indeed exhibit non-relativistic spin-splitting due to two nonequivalent sublattices with antiparallel magnetic moments. The optical conductivities have been calculated and converted into permittivities, based on which we have found optical nonreciprocity and hyperbolicity. Nonreciprocity is caused by the AHCs, which is assured by the symmetry breaking, while hyperbolicity can be ascribed to the localized d orbitals in Mn, where both spin-up and spin-down conductivities contribute. Based on our investigations, altermagnetic MnF_2 and other materials with similar symmetries have rich optical properties and may have fascinating applications in optics.

Acknowledgement

Project supported by Hangzhou Dianzi University (Grant No. KYS075621018).

References

[1] Bai L, Feng W, Liu S, Šmejkal L, Mokrousov Y and Yao Y 2024 2024 *Adv. Funct. Mater.* **34** 2409327
[2] Fender S S, Gonzalez O and D K Bediako 2025 *J. Am. Chem. Soc.* **147** 2257
[3] Song C, Bai H, Zhou Z, Han L, Reichlova H, Hugo Dil J, Liu J, Chen X and Pan F 2025 *Nat. Rev. Mater.* **10** 473
[4] Šmejkal L, Sinova J and Jungwirth T 2022 *Phys. Rev. X* **12** 040501
[5] Bose A, Schreiber N J, Jain R, Shao D F, Nair H P, Sun J, Zhang X S, Muller D A, Tsymbal E Y, Schlom D G and Ralph D C 2022 *Nat. Electron.* **5** 267
[6] Bai H, Han L, Feng X Y, Zhou Y J, Su R X, Wang Q, Liao L Y, Zhu W X, Chen X Z, Pan F, Fan X L and Song C 2022 *Phys. Rev. Lett.* **128** 197202

[7] Karube S, Tanaka T, Sugawara D, Kadoguchi N, Kohda M and Nitta J 2022 *Phys. Rev. Lett.* **129** 137201

[8] Cao R, Dong R, Fei R and Yao Y 2024 arXiv: 2412.20347

[9] Guo W T, Xu J, Yang Y, Zhang H and Wang H 2025 arXiv: 2505.01964

[10] Xie C, Meng W, Guo Z, Wang W, Zhou X, Qian S, Cheng Z and Wang X 2025 arXiv: 2508.12770

[11] Zhu Z, Liu Y, Duan X, Zhang J, Hao B, Wei S H, Zutic I and Zhou T 2025 arXiv: 2507.07039

[12] Reimers S, Odenbreit L, Šmejkal L, Strocov V N, Constantinou P, Hellenes A B, Ubiergo R J, Campos W H, Bharadwaj V K, Chakraborty A, Denneulin T, Shi W, Dunin-Borkowski R E, Das S, Kläui M, Sinova J and Jourdan M 2024 *Nat. Commun.* **15** 2116

[13] Yang G, Li Z, Yang S, Li J, Zheng H, Zhu W, Pan Z, Xu Y, Cao S, Zhao W, Jana A, Zhang J, Ye M, Song Y, Hu L H, Yang L, Fujii J, Vobornik I, Shi M, Yuan H, Zhang Y, Xu Y and Liu Y 2025 *Nat. Commun.* **16** 1442

[14] Reichlova H, Seeger R L, González-Hernández R, *et al.* 2024 *Nat. Commun.* **15** 4961

[15] Sato T, Haddad S, Fulga I C, Assaad F F and van den Brink J 2024 *Phys. Rev. Lett.* **133** 086503

[16] Poddubny A, Iorsh I, Belov P and Kivshar Y 2013 *Nat. Photon.* **7** 948

[17] Jacob Z, Smolyaninov I I and Narimanov E E 2012 *Appl. Phys. Lett.* **100** 181105

[18] Cortes C L, Newman W, Molesky S and Jacob Z 2012 *J. Optics* **14** 063001

[19] Liu Z, Lee H, Xiong Y, Sun C and Zhang X 2007 *Science* **315** 1686

[20] Rho J, Ye Z, Xiong Y, Yin X, Liu Z, Choi H, Bartal G and Zhang X 2010 *Nat. Commun.* **1** 143

[21] Ishii S, Kildishev A V, Narimanov E, Shalaev V M and Drachev V P 2013 *Las. Photon. Rev.* **7** 265

[22] Fang A, Koschny T and Soukoulis C M 2009 *Phys. Rev. B* **79** 245127

[23] Lee D, So S, Hu G, Kim M, Badloe T, Cho H, Kim J, Kim H, Qiu C W and Rho J 2022 *eLight* **2** 1

[24] Chen X, Liu Y, Liu P, Yu Y, Ren J, Li J, Zhang A and Liu Q 2025 *Nature* **640** 349

[25] Morano V C, Maesen Z, Nikitin S E, Lass J, Mazzone D G and Zaharko O 2025 *Phys. Rev. Lett.* **134** 226702

[26] Zhu Z, Duan X, Zhang J, Hao B, Žutić I and Zhou T 2025 *Nano Lett.* **25** 9456

[27] Zhou J and Zhang C 2025 *Phys. Rev. Lett.* **134** 176902

[28] Giannozzi P, Baroni S, Bonini N, *et al.* 2009 *J. Phys.: Condens. Matter* **21** 395502

[29] Giannozzi P, Andreussi O, Brumme T, *et al.* 2017 *J. Phys.: Condens. Matter* **29** 465901

[30] Giannozzi P, Baseggio O, Bonfà P, Brunato D, Car R, Carnimeo I, Cavazzoni C, de Gironcoli S, Delugas P, Ruffino F F, Ferretti A, Marzari N, Timrov I, Urru A and Baroni S 2020 *J. Chem. Phys.* **152** 154105

[31] Hamann D R 2013 *Phys. Rev. B* **88** 085117

[32] Pizzi G, Vitale V, Arita R, Blügel S, *et al.* 2020 *J. Phys.: Condens. Matter* **32** 165902

[33] Li Y H, Zhan Z, Kuang X, Li Y and Yuan S 2023 *Comput. Phys. Commun.* **285** 108632

[34] https://cn.comsol.com/

[35] Yu G X, Fu J J, Du W W, Lv Y H, Luo M 2019 *Chin. Phys. B* **28** 024101